# Increased Blood Flow and Oxidative Metabolism in the Human Brain by Transcranial Laser Stimulation

Greg M. Dmochowski[1], Jacek P. Dmochowski[2*]

**1 Princess Margaret Cancer Centre, Toronto, Ontario M5G 1L7, Canada**
**2 Department of Biomedical Engineering, 160 Convent Avenue, New York, NY 10031, USA**

**\* jdmochowski@ccny.cuny.edu**

## Abstract

The non-invasive delivery of laser light to the brain, termed transcranial photobiomodulation (tPBM), has been shown to stimulate vascular and metabolic function in the rodent brain. Given the large number of neurological disorders marked by impaired blood flow and metabolism, it is important to objectively evaluate the reported effects in humans. To date, however, neurophysiological evidence of tPBM effects in the human brain is scarce. Here we combined tPBM with functional magnetic resonance imaging (fMRI) by recording the blood-oxygenation-level dependent (BOLD) signal before, during, and after application of tPBM to the right forehead of 20 healthy participants. We found both acute and outlasting BOLD increases as high as 31% in regions of the prefrontal cortex within 30 mm of the site of light incidence. The observed effect was consistent with rapid inflow of blood to the stimulated brain region, coupled with an increase in oxidative metabolism. Our findings underscore the therapeutic potential of tPBM in the human brain.

## Introduction

Ever since Endre Mester serendipitously discovered that low-levels of coherent light stimulate hair growth in mice [41], the delivery of light to tissue for therapeutic purposes - now known as photobiomodulation (PBM) - has been investigated for an array of conditions, including wound healing and joint pain reduction [14]. Intriguingly, PBM has recently shown promise as a treatment for disorders of the central nervous system, including both neurological (e.g. stroke, traumatic brain injury) and psychiatric (e.g. depression) disorders [24]. The purported mechanism of action in transcranial PBM (tPBM) is the absorption of light by cytochrome $c$ oxidase (CCO), the terminal enzyme in the mitochondrial electron transport chain, leading to increased energy metabolism [12]. Absorption of near-infrared light has been hypothesized to upregulate CCO activity and increase the rate of ATP production [33,62], which could then fuel a number of neuronal processes [4].

Several findings from animal and cell culture models support the idea that near-infrared light boosts brain metabolism. tPBM has been shown to increase cerebral blood flow (CBF) [60] and cortical ATP [42], while reducing reducing inflammatory markers [43, 66] and apoptosis [53, 62, 65]. Moreover, tPBM has been reported to ameliorate amyloid beta induced neurodegeneration [37] and oxidative damage from sleep deprivation [54]. Translation of these findings to human neurology and psychiatry

has the potential to yield new treatments for disorders in which metabolic or vascular dysfunction have been implicated (e.g. Alzheimer's Disease [22], depression [6]).

However, there are significant cross-species differences in skull thickness and head size, and it is unknown whether tPBM similarly modulates biological processes when applied through the thicker human cranium and when stimulating only a portion of the brain. Moreover, the measurement of CBF and cerebral blood oxygenation in humans is presently only possible with neuroimaging, whose sensitivity is lower than the invasive techniques employed in animal studies. In order to assess the potential therapeutic benefits of tPBM, objective neurophysiological evidence of its effects on the human brain are necessary.

To date, however, human investigations of tPBM have largely employed cognitive and behavioral outcome measures. Improvements in sustained attention and working memory after a single session of tPBM have been reported [5, 30]. Recent investigations have found that tPBM improves rule-based learning [8] and performance on tests of executive function [7]. Neurophysiological changes in the human brain have only been probed with near infrared resonance spectroscopy (NIRS), reporting an increase in oxygenated hemoglobin over both cerebral hemispheres following application to the right forehead [59]. Due to absorption and scattering of light through the human head, NIRS is limited in its spatial resolution and the ability to measure deep structures [23]. Functional magnetic resonance imaging (fMRI), on the other hand, confers excellent spatial resolution and the ability to image proxies of brain metabolism. In particular, the blood-oxygenation-level-dependent (BOLD) signal is sensitive to both CBF and the cerebral metabolic rate of oxygen ($CMRO_2$) [10], processes that are expected to vary along with a local change in energy metabolism.

fMRI measures the level of deoxygenated hemoglobin in a small volume of tissue. Its vast use in studies of brain function stems from the basic finding that during neural activation, there is an increase in CBF that outweighs the activation-driven increase in oxidative metabolism [45]. Consequently, the relative level of deoxyhemoglobin is actually *decreased* during activation, leading to an increased BOLD signal due to a more homogeneous local magnetic field [10]. Conventional BOLD imaging samples the T2* decay only once ("single-echo"), whereas multi-echo BOLD acquires multiple (usually 3) samples, with the BOLD contrast from neural activation *increasing* with echo time [34, 49]. Importantly, the initial (zero-echo) signal intensity is sensitive only to perfusion and independent of deoxygenated hemoglobin content [35].

Here we conducted the first human brain imaging study of tPBM by recording the multi-echo BOLD signal from $N = 20$ healthy participants receiving tPBM to the right forehead. We found a significant increase in BOLD at brain regions predicted to have high absorption by a simulation of light propagation through the human head. The effect persisted beyond the stimulation period, appearing at all three echos and *decreasing* in magnitude with echo time.

# Results

**Simulation of light propagation predicts substantial absorption in grey matter.** In order to estimate the spatial extent of significant light absorption in the human brain, we simulated photon propagation through a heterogeneous medium whose optical properties matched those of the human head. The model consisted of four infinitely-wide slabs corresponding to the scalp, skull, cerebrospinal fluid, and brain (Fig 1A; see *Simulating light propagation*). Although the model did not account for the real geometry of the head, we expected its predictions to be reasonable due to the small size of the beam (i.e., 1 cm diameter) in relation to the curvature of the human scalp. The total simulated dose (150 J) applied to the model matched that of the experiments. The

simulated absorption exhibited a maximum in the scalp and decreased exponentially with depth (Fig 1B, logarithmic colormap). Interpolating the absorption pattern onto the anatomical MRIs of the study participants led to maxima in the grey and white matter of $0.83 \pm 0.18$ J/cm$^3$ (standard deviation across $N = 20$ subjects) and $0.49 \pm 0.13$ J/cm$^3$, respectively (Fig 1C; see "*Interpolating light absorption onto human head*"). The total absorption within the grey and white matter totaled $0.88 \pm 0.19$ J and $0.36 \pm 0.10$ J, respectively (Fig 1D). Thus, despite the thickness of the human cranium, substantial light absorption is expected in the cerebral cortex.
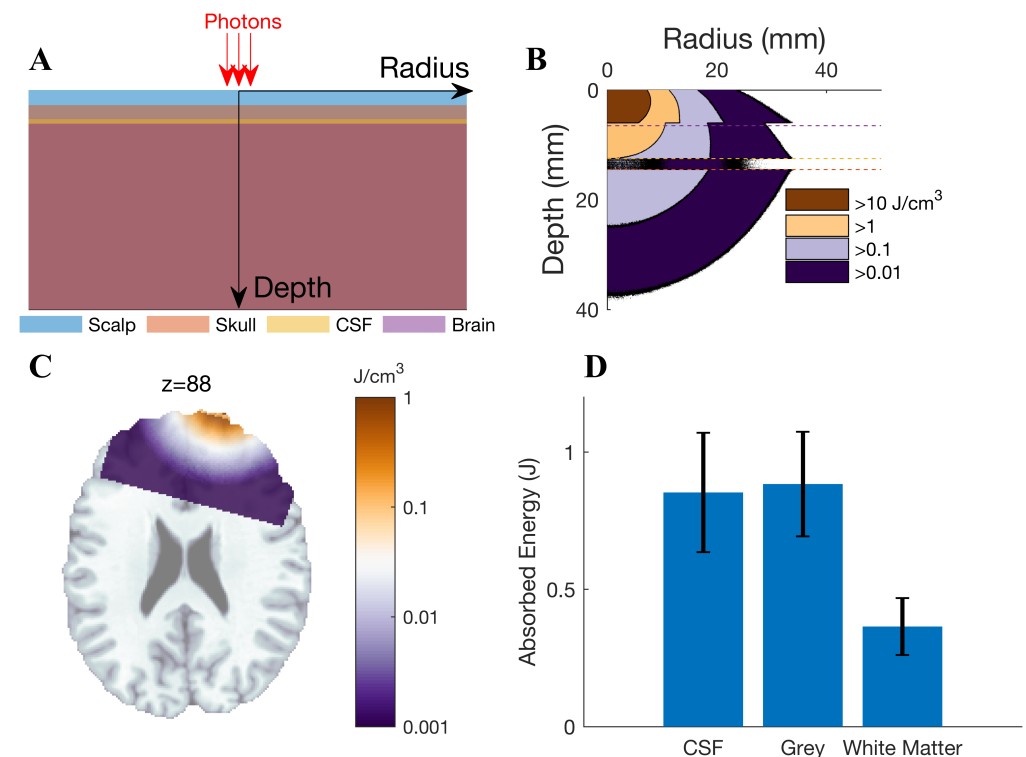
70
71
72
73
74
75
76
77



**Figure 1.** Simulation of light propagation predicts substantial absorption in cortex. (**A**) Four-slab model used to simulate transcranial delivery of near-infrared light to the human brain. Photons enter the scalp and are reflected, scattered, and/or absorbed in a stochastic manner. (**B**) The predicted absorption pattern exhibited a maximum in the scalp and decayed exponentially, showing discontinuities at tissue boundaries. (**C**) Projection of the absorption pattern onto the anatomical MRI of a template brain. Peak absorption values in the brain were $0.83 \pm 0.18$ J/cm$^3$ (standard deviation across $N = 20$ individual MRIs). (**D**) Integrating across the brain, a total of $0.88 \pm 0.19$ J of light energy was absorbed by the grey matter during simulated tPBM whose parameters matched the experiments.
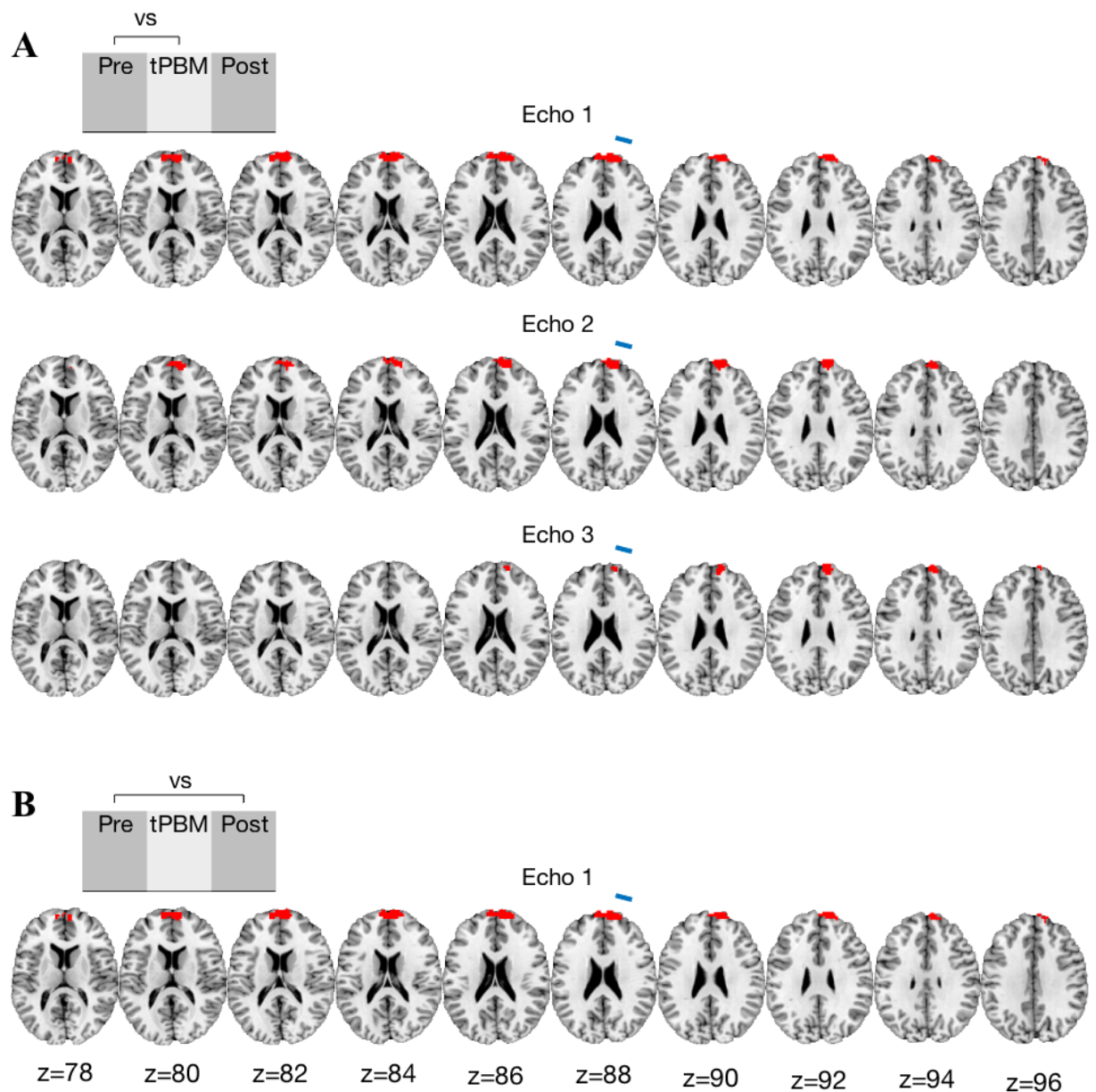
**Figure 2. tPBM produces acute and outlasting effects on the BOLD signal.** (**A**) Axial brain slices showing voxels (in red) exhibiting statistically significant differences in BOLD during tPBM, relative to the pre-tPBM period. A cluster of 214 voxels was found in the right medial frontal gyrus (MFG), 24 mm from the site of light incidence (voxel-wise Chow test, corrected for multiple comparisons by controlling the False Discovery Rate at $\alpha <0.05$). Significant clusters were also detected at Echo 2 (right MFG, 22 mm) and Echo 3 (right superior frontal gyrus, 23 mm). (**B**) Same as A but now depicting the brain regions whose BOLD differed significantly between the pre- and post-tPBM periods. A cluster centered in the left MFG was detected at the first echo, 29 mm from the laser. No significant clusters near the laser were detected for echos 2 and 3. The location and orientation of the laser are marked in blue.

**Modulation of BOLD at multiple echos.** To determine whether tPBM modulated the BOLD signal, and if so, over what extent of the brain, we conducted a whole-brain analysis, probing for both acute and outlasting effects. Statistical Chow tests [13] were conducted separately at each echo of the group-averaged BOLD in order to detect

| | Pre- vs Peri-tPBM | | | | | | Pre- vs Post-tPBM | | | | | |
| | Center of Mass | | | Dist. | Volume | Atlas | Center of Mass | | | Dist. | Volume | Atlas |
| | x (mm) | y (mm) | z (mm) | (mm) | (mm³) | | x (mm) | y (mm) | z (mm) | (mm) | (mm³) | |
| Echo 1 | | | | | | | | | | | | |
| | -5.7 | -59.1 | 19.9 | 23.8 | 3344 | (R) MFG | 0.5 | -59.1 | 20.3 | 28.7 | 3406 | (L) MFG |
| | | | | | | | 18.5 | 40.6 | 53.8 | 127.0 | 656 | (L) PCL |
| Echo 2 | | | | | | | | | | | | |
| | -9.3 | -57.6 | 20.9 | 22.4 | 2406 | (R) MFG | | | | | | |
| Echo 3 | | | | | | | | | | | | |
| | -1.6 | 9.7 | 46.2 | 90.7 | 1203 | (R) PCL | -34.3 | 56.3 | -47.7 | 149.3 | 656 | (R) CER |
| | 1.7 | 50.6 | -22.6 | 135.8 | 984 | (L) CER | | | | | | |
| | -10.7 | -56.8 | 26.1 | 22.5 | 875 | (R) SFG | | | | | | |
| | -33.4 | 54.0 | -46.6 | 146.7 | 625 | (R) CER | | | | | | |

**Table 1.** Clusters of voxels exhibiting statistically significant BOLD changes during tPBM relative to the pre-stimulation period (left panel) and after tPBM relative to the pre-stimulation period (right panel). Blue shading indicates brain regions within 3 cm of the site of light incidence. MFG: medial frontal gyrus; SFG: superior frontal gyrus; CER: cerebellum; PCL: paracentral lobule

significant changes during and after tPBM, relative to the pre-stimulation baseline period. The Chow test detects structural changes between two time series (here implemented by comparing two sets of autoregressive (AR) coefficients; see *Chow Test for detecting an effect on BOLD*), thus representing a more flexible test of significant differences between temporal data records than, for example, comparing the levels of the signals.

During tPBM, we found a significant modulation of early-echo (13 ms) BOLD in a cluster of 214 voxels in the right medial frontal gyrus (MFG), 24 mm from the site of light incidence (Fig 2A). A cluster of 154 voxels in the right MFG, 22.4 mm from incidence, was also found at echo 2 (34 ms). Four smaller clusters were detected at echo 3 (56 ms), including one in the right superior frontal gyrus (SFG), 22.5 mm from incidence. The other 3 clusters were located in the paracentral lobule (includes the motor cortex) and cerebellum (>90 mm from the laser), likely reflecting increased movement and movement control during tPBM (study participants were asked to remain still for a 30 minute duration).

Interestingly, we found that tPBM produced an effect on the early-echo BOLD that outlasted the stimulation. A cluster of 218 significant voxels centered in the MFG was found at a distance of 28.7 mm from incidence (Fig 2B). Outlasting effects were also detected in smaller clusters of the paracentral lobule (echo 1) and cerebellum (echo 3). The locations of all significant clusters, for both acute and outlasting effects, are listed in Table 1.

**tPBM increases low-frequency BOLD.** The Chow test detects structural changes in a time course, but is agnostic to what those changes are. In order to determine the nature of the BOLD effect induced by tPBM (i.e., increase versus decrease, low versus high-frequency), we examined the time courses and AR spectra of the BOLD at the voxels marked significant by the Chow test. Changes to the AR spectrum of the BOLD shed light into which frequencies were modulated (see *"Computation of AR spectrum"*).

The average time course of significant voxels did not exhibit sustained level differences either during or after tPBM relative to baseline for any of the echos (Fig 3A). Instead, the tPBM effect was evident when examining the spectral content of the BOLD. During stimulation, the AR spectra showed a marked increase in low frequency power for all echos, with the magnitude of the effect decreasing with echo (Fig 3B). The largest increase was observed near DC (0 Hz), indicating a slow modulation from tPBM. The low-frequency increases persisted after stimulation, albeit to a lesser extent than that observed during tPBM (i.e., spectra fell closer to baseline values). We also examined the AR spectra of the voxels *not* marked significant by the Chow test. These spectra showed

remarkable consistency across the pre-tPBM, peri-tPBM, and post-tPBM segments (Fig 3C).

In order to quantify the magnitude of the observed BOLD effect, we computed a measure of percent signal change from the AR spectra. To that end, we computed a frequency-weighted average of percent signal change using the baseline AR power for the frequency weighting. For the acute tPBM effects, the resulting percent signal changes were 31%, 26%, and 11% for echos 1, 2, and 3, respectively (Fig 3D). tPBM produced *outlasting* percent signal changes of 25%, 16%, and 3% for echos 1, 2, and 3, respectively.
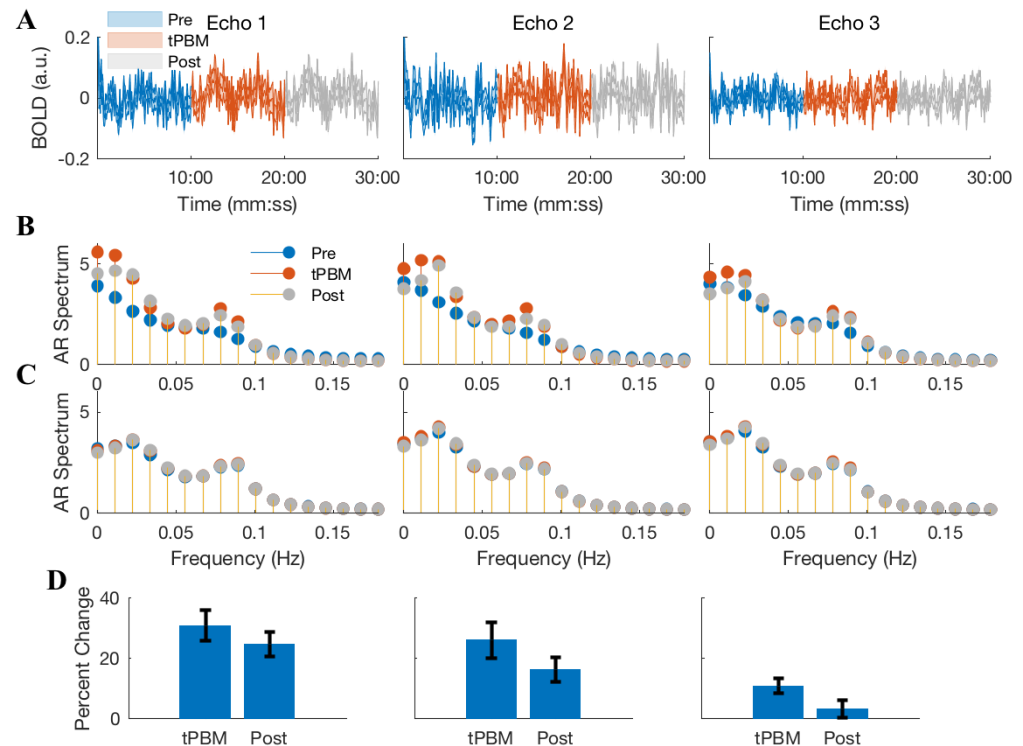


**Figure 3.** tPBM increases low-frequency BOLD during and after stimulation. (**A**) The group BOLD time course at voxels marked significant by the parametric Chow test (pre-tPBM: green; peri-tPBM: red; post-tPBM: grey). Sustained level differences were not observed for any of the 3 echos. Shading denotes standard deviations across 100 bootstrap replicates of the group BOLD. (**B**) During tPBM, the average AR spectra of significant voxels showed a marked increase in low-frequency power at all 3 echos. The effect was largest at echo 1 and smallest at echo 3. The increase in low-frequency BOLD was sustained, albeit to a lesser extent, following tPBM. (**C**) Average AR spectra of the remaining (non-significant) voxels showed strong consistency across the pre-, peri-, and post-tPBM windows. (**D**) Averaged across frequencies, acute BOLD changes had magnitudes of 31, 26, and 11% for echos 1, 2, and 3, respectively, while outlasting changes were 25, 16, and 3%. Error bars denote standard deviations across 100 bootstrap replicates.

**BOLD effect decreases linearly with echo.** To gain insight into the physiological mechanisms bringing about the observed changes in BOLD, we analyzed the magnitude of the effect as a function of echo time: the early echo signal is only sensitive to CBF, whereas the slope of the percent change across echo time indicates whether the level of deoxygenated venous blood increased or decreased [34, 49]. We thus regressed the

percent signal change (see Fig 3D) onto echo time, considering only the voxels exhibiting a significant effect at any of the three echos (Fig 4A; $N = 258$). Averaging across all such voxels, we found a *decreasing* linear trend in the percent signal change across echo time (Fig 4B; $R^2 = 0.99$, $p = 0.084$, $F = 69.7$, $n = 3$).
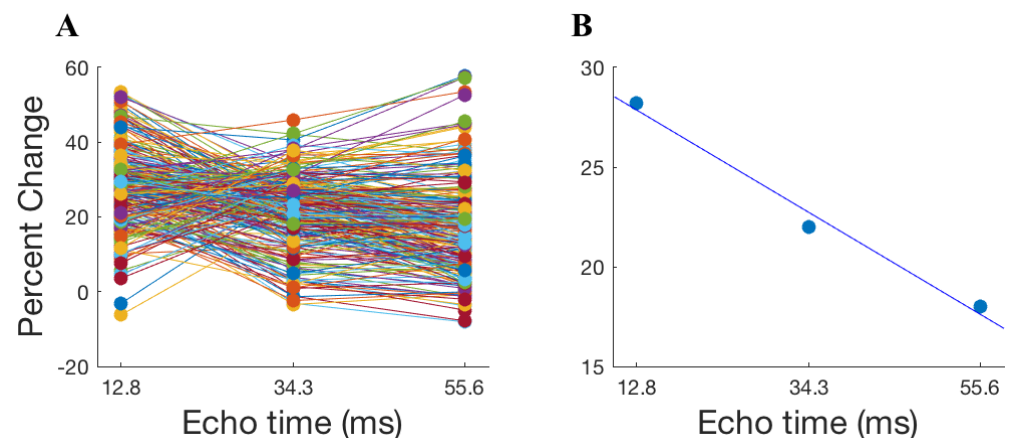


**Figure 4.** BOLD signal change decreases linearly with echo time. (**A**) The percent signal change at all voxels exhibiting a significant BOLD change, shown as a function of echo time. Each plot depicts a single voxel. (**B**) Averaging across all significant voxels, the percent signal change showed a linear trend with echo time ($F = 69.7$, $p = 0.084$, $n = 3$, $R^2 = 0.99$).

**Estimating energy required to modulate BOLD.** Having both the predicted absorption levels (Fig 1) and the spatial pattern of modulated voxels throughout the brain (Fig 2), we sought to estimate the amount of light needed to produce a significant effect on BOLD. For this we separated the voxels into those that responded to tPBM and those that did not. For all 3 echos, the absorption distributions of the two classes showed a high amount of separability (Fig 5A), with the absorption of responsive voxels (means of 0.15 J/cm$^3$, 0.17 J/cm$^3$, and 0.19 J/cm$^3$ for echos 1, 2, and 3 respectively) greatly surpassing those of the non-responsive voxels (means of 0.008 J/cm$^3$, 0.008 J/cm$^3$, and 0.01 J/cm$^3$). Employing the logistic regression framework (Nedler and McCullers, 1986), we were able to achieve nearly perfect linear classification of responsive versus non-responsive voxels based on the absorption (Fig 5B, Area Under ROC curve = 0.97, 0.98, and 0.99 for echoes 1, 2, and 3, respectively). The decision boundaries were 0.01, 0.03, and 0.04 J/cm$^3$ at echos 1, 2, and 3. Importantly, the absorptions at which the probability of a significant effect exceeded 0.95 were found to be 0.10, 0.10, and 0.11 J/cm$^3$ for echos 1, 2, and 3, respectively. These values may be interpreted as the amount of absorbed light that is required to produce a reliable effect on BOLD.
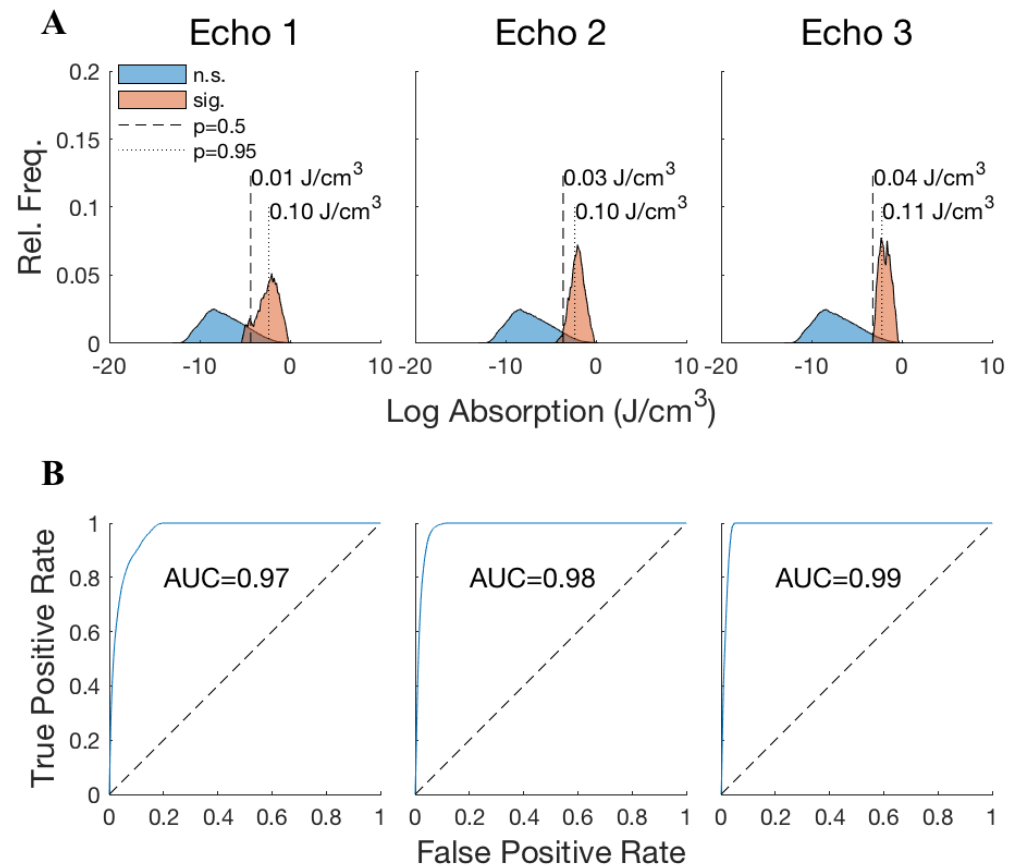
**Figure 5.** tPBM modulates BOLD with 0.1 J/cm$^3$. (**A**) Voxels were separated into those that showed a significant BOLD effect (orange distribution) and those that did not (blue). The absorption values of the two classes showed a clear separability at all 3 echos. Logistic regression was used to optimally classify responsiveness to tPBM from the predicted absorption value. The optimal decision thresholds (that which yields equal probabilities for the two classes) were found to be 0.01, 0.03, and 0.04 J/cm$^3$ for echos 1, 2, and 3, respectively. Moreover, the absorptions at which the model predicted a probability of significant modulation of over 0.95 were 0.1, 0.1, and 0.11 J/cm$^3$, suggesting that this amount of light must be absorbed at a given location to modulate the BOLD signal. (**B**) Nearly perfect linear classification of voxel response to tPBM was achieved, with the area under the ROC curve exceeding 0.97 for all 3 echos.

# Discussion

By applying tPBM to human participants concurrently to scanning their brain activity with multi-echo fMRI, we found that non-invasive laser stimulation of the brain produced acute and outlasting changes to the BOLD signal. A low-frequency increase in the AR spectrum was observed in the medial and superior frontal gyri (MFG/SFG) within 30 mm of the site of light incidence. The increase in BOLD was largest at echo 1 (31%) and decreased linearly with echo time (26% and 11% in echos 2 and 3, respectively).

Our findings are consistent with a superposition of two distinct physiological effects. The first is an increase in CBF, as evidenced by the large BOLD increase at an early echo (i.e., 13 ms) at which the effect of oxygenation is nearly zero [35, 49]. The increased perfusion manifests as an apparent T1 effect where fresh blood enters the imaging voxel and increases the initial signal intensity of the $T2^*$ signal [21]. Importantly, the contribution of the blood inflow to BOLD signal changes is constant across echo [34]. The second effect is a simultaneous increase in oxidative metabolism, as evidenced by the fact that the magnitude of the net BOLD effect decreased linearly with echo time (see Fig 4). This indicates that the increase in CBF was coupled with a relatively *larger* increase in $CMRO_2$, thus yielding an overall increase in the oxygen extraction fraction (OEF), defined as the ratio of $CMRO_2$ to CBF weighted by the arterial oxygen concentration [10]. Thus, our findings indicate that tPBM achieved a focal increase in blood perfusion coupled with a larger increase in oxidative metabolism. To illustrate the superposition of these two inferred effects, we have performed a simulation of the BOLD where simultaneous increases of CBF and OEF were modeled (Fig S2). Note that the fact that after-effects were only observed at echo 1 actually suggests that outlasting changes occurred to both perfusion and oxygenation. At echos 2 and 3, the increase in deoxygenated venous blood reduced the overall BOLD to baseline values, leading to a non-significant net effect.

In studies of brain activation, the BOLD effect arises from a mismatch between CBF and $CMRO_2$: neural activation produces an increase in oxidative metabolism along with an even larger increase in blood flow [10]. As the BOLD signal is sensitive to the homogeneity of the local magnetic field, the relative decrease of paramagnetic deoxygenated venous blood increases the $T_2^*$ signal. On the other hand, the effect observed here was marked by an increase in deoxygenated hemoglobin that went uncompensated by CBF. Moreover, the effect of perfusion that was found here to increase initial signal intensity is apparently not observed in studies of neural activation, which employ echo times in the order of 30 ms (closest to our second echo time). Thus, we observed two phenomena distinct from those found during neural activation studies: rapid perfusion that increased initial signal intensity, and an increase in $CMRO_2$ that outweighed the effects of CBF, leading to decreasing BOLD across echo time.

The difficulties of interpreting the single-echo BOLD signal are evident when considering our findings from the middle echo in isolation (i.e., 34 ms). In this hypothetical case, one would interpret the finding as a BOLD increase and hence incorrectly infer a relative increase in CBF that outweighed $CMRO_2$ (as in neural activation). However, the availability of the two additional echos allowed us to determine that in fact the $CMRO_2$ increased more than CBF, and that the net increase was due to the apparent T1 decrease from an inflow of blood into the imaging slice. In this manner, our study illustrates the importance of multi-echo BOLD in developing a quantitative understanding of the underlying physiological changes. Moreover, it suggests that caution should be exercised when interpreting single-echo BOLD effects.

Our findings are consistent with the absorption of near infrared light by mitochondrial CCO, leading to increased ATP production. The increased metabolism would manifest as an increase in the $CMRO_2$, which would in turn yield increased CBF into the stimulated region. A rapid increase of CBF that did not fully compensate for the $CMRO_2$ increase

could then produce the BOLD changes observed here. However, it is important to point ²¹¹
out that the observed effects on BOLD may also have come about from an effect of ²¹²
heating. The rates of chemical reactions, including oxidative metabolism in the brain, ²¹³
are temperature dependent. The heating of brain tissue that is expected to occur during ²¹⁴
tPBM may increase local $CMRO_2$. The increased metabolic rate will then decrease the ²¹⁵
oxygen saturation in the venous blood and hence decrease the BOLD signal. Under ²¹⁶
this scenario, if the CBF recruited to cool the tissue with an inflow of cooler arterial ²¹⁷
blood was not sufficient to counteract the evoked increase in $CMRO_2$, then the BOLD ²¹⁸
effects observed here would be predicted. During prolonged visual stimulation that ²¹⁹
increased the BOLD by approximately 5%, tissue temperature *decreases* of 0.2° have ²²⁰
been estimated in the brain [63]. Incidentally, under the assumption that all of the ²²¹
absorbed light from tPBM ends up as heat, we estimate that the peak temperature ²²²
increase in the grey matter was also 0.2° (see *"Estimating heating induced by tPBM"*). ²²³
The processes regulating temperature in the brain are not well understood, and it is ²²⁴
difficult to predict how an exogenous increase in brain temperature would alter the ²²⁵
dynamics of CBF and $CMRO_2$. We note, however, that our findings cannot be explained ²²⁶
by a simple cooling effect of increased CBF to remove the exogenous heat from tPBM. ²²⁷
This would be marked by increased CBF ($CMRO_2$ unchanged) which would increase ²²⁸
BOLD but in a manner that increases linearly with echo time (here we found a decrease ²²⁹
with echo). ²³⁰

Regardless of the mechanism of action, the ability to non-invasively increase perfusion ²³¹
and metabolism in the human brain encourages the investigation of light-based approaches ²³²
to the treatment of neurological and psychiatric disorders associated with impaired CBF ²³³
or metabolism. Most notably, it has been argued that Alzheimer's Disease (AD) is a ²³⁴
cerebrovascular pathology, with chronic brain hypoperfusion linked to AD risk factors ²³⁵
and preclinical detection [16]. Intriguingly, there is also evidence that mitochondrial ²³⁶
dysfunction has an early role in the progression of AD [44]. tPBM has already been ²³⁷
shown to reduce Amyloid Beta ($A\beta$) plaque levels in a transgenic mouse model of ²³⁸
AD [17]. Moreover, laser stimulation of the mouse tibia bone marrow reduced $A\beta$ ²³⁹
deposition in progressive AD stages [19]. Taken together with these promising findings ²⁴⁰
from animal studies, our results compel the investigation of tPBM in the treatment and ²⁴¹
prevention of human AD. The design of such trials will necessitate carefully selecting ²⁴²
several parameters, including the site of stimulation on the scalp. Note that in rodent ²⁴³
models, the diameter of the laser beam is on the same order as the entire dorsal cortical ²⁴⁴
surface [17]. The results of the mouse bone marrow study [19] suggest that circulation ²⁴⁵
may transfer PBM effects to the brain, although we did not find any "network" effects ²⁴⁶
in this transcranial stimulation study. ²⁴⁷

One potential limitation of tPBM pertains to the penetration depth. Here we found ²⁴⁸
effects on brain regions within 3 cm of the site of light incidence. This empirical ²⁴⁹
finding matched the prediction of our light propagation model, and we estimated that ²⁵⁰
approximately 0.1 $J/cm^3$ was required to achieve a reliable effect on BOLD. An absorbed ²⁵¹
energy density of 0.1 $J/cm^3$ corresponds to a fluence of 1.2 $J/cm^2$ in the brain. Biphasic ²⁵²
dose responses have been reported for PBM [29], with maxima near 3 $J/cm^2$ [25]. Based ²⁵³
on our model, the maximum deposited energy density in the grey matter was 0.83 $J/cm^3$, ²⁵⁴
corresponding to a fluence of 9.9 $J/cm^2$. An observed BOLD effect at these fluences ²⁵⁵
is, therefore, in line with previously reported efficacious doses. Brain regions such as ²⁵⁶
the dorsolateral prefrontal cortex (DLPFC), a frequent target for transcranial magnetic ²⁵⁷
stimulation (TMS) [47], appear to be well within the reach of tPBM. To reach subcortical ²⁵⁸
regions such as the subthalamic nucleus [36] and hippocampus [51], targets for other ²⁵⁹
forms of brain stimulation, it may be required to employ multiple applicators such that ²⁶⁰
the net absorption in these deep targets reaches the threshold found here. ²⁶¹

Finally, our findings extend the recent body of evidence showing that light stimulation ²⁶²

modulates physiological processes in diverse ways. Blue light has been shown to increase CBF by dilating arterial vessels [52], introducing potential confounds in studies combining optogenetics and fMRI. In a similar light, our findings suggest that caution should be exercised when interpreting NIRS measurements, especially those made over long periods of time where significant absorption of light may have increased perfusion and oxidative metabolism *per se*. Pulsed infrared stimulation has been shown to alter the electrical capacitance of oocytes via absorption of photons by water [57]. Here we applied light transcranially to the intact human brain, thus hinting that such physiological effects may be achieved non-invasively and in humans.

# Acknowledgments

# Materials and Methods

**Subjects.** All study procedures were approved by the Institutional Review Board of the City University of New York. We recruited $N = 20$ participants (10 females) from the local New York City population. In an attempt to achieve uniform baseline measures of cerebral oxygenation in our sample, only subjects aged 18-40 were considered: the cerebral metabolic rate of oxygen ($CMRO_2$) has been found to decrease monotonically with age [39, 64]. The mean age of the participants was $24.8 \pm 4.6$ years. During recruitment, we employed those exclusionary criteria common to MRI (e.g., patients with cardiac pacemakers, neurostimulation systems, or claustrophobia were excluded). All subjects completed the experiments and there were no major adverse effects. One subject complained of a headache following the scan, which may have been caused by the headgear that was worn throughout the ($\sim$1 h) experiment.

**Experimental Design.** We employed a within-subjects design where the BOLD signal was continuously acquired for 30 minutes. The laser was turned on 10 minutes after the onset of the scan and remained active for a 10-minute duration. The equal durations of the pre-tPBM, peri-tPBM and post-tPBM segments were designed to allow a consistent and reliable measure of BOLD during the three experimental periods. Subjects were not made aware of when the laser was turned on or for how long. From verbal post-experimental surveys, subjects did not perceive any sensations (thermal or otherwise) during tPBM.

**Transcranial Laser Stimulation.** Participants received tPBM at a wavelength of 808 nm, selected based on a previous study that demonstrated an improvement in cognitive task performance after tPBM in healthy volunteers [5]. This wavelength falls within the so-called "optical window" in which absorption by common chromophores (water, melanin, and hemoglobin) is low [26], allowing for deeper penetration through the human scalp and skull and into the brain as compared to other candidate wavelengths [48, 58].

A class IV 10W diode laser (Ultralasers MDL-N-808-10000) powered by a laser driver (Ultralasers PSU-H-LED) provided the monochromatic light. A calibrated photodetector

was employed to set the laser power to 250 mW prior to each experiment; the output power of the laser varied by less than 1%. Given a 1 cm diameter aperture in the headgear worn by participants, this resulted in an intensity of 318 mW/cm$^2$, which is within the ANSI safety limit for human tissue (330 mW/cm$^2$).

The laser output was coupled directly into a custom made, multimode optical fiber (Thorlabs FT400EMT) whose core diameter was 400 $\mu$m. In order to ensure MR compatibility, the distal end of the optical fiber was fitted with a ceramic ferrule, which was affixed to a custom 3D-printed headgear worn by participants. The headgear, measuring 5.5 cm x 3.2 cm x 2.7 cm, contained a clamp which secured the ferrule. The headgear was secured against the subject's head such that its 1 cm diameter aperture was flush against the forehead. Given that the duration of tPBM was set to 10 minutes, the total incident light energy was 150 J. It should be noted that the coherent nature of the laser is not believed to contribute to any of the observed effects. A given photon undergoes multiple scattering events on its path to the brain, thereby losing its original phase information. Light emitting diodes (LEDs) have elicited effects in previous PBM experiments [14]. A laser was employed in this case to facilitate light delivery at the desired power.

The headgear was centered at location "Fp2" (right frontal pole) of the 10/20 standard system for electroencephalography [32], where each participant's Fp2 location was measured and marked on the scalp prior to the experiment. Stimulating the forehead yields better penetration through the scalp due to the absence of scattering by the hair. Our targeted scalp location also matched that employed previously [5]. For all but 2 subjects, Vitamin E markers were placed on the headgear so that the location of light incidence could be registered with the antomical MRI.

**Simulating light propagation** We have used the freely available Monte Carlo Multi Layered (MCML) program [61] to simulate light propagation through the human head. The software models an infinitely narrow photon beam normally-incident on multiple layers (slabs) of turbid material. Each layer is specified by five properties: thickness, refractive index, absorption coefficient ($\mu_a$), scattering coefficient ($\mu_s$), and the anisotropy factor ($g$). The resulting "impulse response" is then convolved with a user-defined, finite diameter beam (Gaussian or flat-top), yielding the light absorption (in units of J/cm$^3$) across a finite cylindrical coordinate space where cylindrical symmetry is assumed.

The human head was modelled with 4 distinct layers: scalp, skull, cerebrospinal fluid (CSF), and the brain parenchyma. As described above, MCML requires the specification of five optical properties for each layer. The values used in our simulations are summarized in Table S1. References to the literature from which these values have been taken are provided in the table. Whenever possible, we have used *in vivo* optical properties. In particular, while MCML requires separate specification of $\mu_s$ and $g$, *in vivo* values for the reduced scattering coefficient $\mu_s' \equiv \mu_s(1-g)$ and $g$ are more readily available. As such, we have inferred values of $\mu_s$ from reported values of $\mu_s'$ and $g$. The references cited for $\mu_s$ report *in vivo* values of reduced scattering coefficients. All values of $\mu_a$ and $\mu_s$ are in units of cm$^{-1}$.

The incoming light was modelled with a beam of 1 cm diameter and a flat intensity profile. In the experiments, we employed a multimode fiber with a core diameter of 400 $\mu$m to deliver the laser light to the subject's head. The transverse intensity profile of our beam was neither Gaussian nor flat-top. However, simulating a Gaussian beam is expected to underestimate the lateral spread of the light inside the head. We preferred to obtain an upper bound on the lateral distribution and thus modelled the beam with a flat transverse intensity profile. We simulated an input energy of 150 J, corresponding to a 10 minute application of tPBM at an intensity of 250 mW.

A grid spacing of 20$\mu$m was used in both radial and axial directions, and 500,000

photons were simulated in each of five runs. We report the average absorption across the 5 runs.

**Estimation of heating induced by tPBM.** From the simulation of light absorption, the maximum energy absorption in the brain was estimated as $E = 0.83$ J/cm$^3$. To relate this to a change in tissue temperature, we employed average values of specific heat capacity [1] and density [2] of grey matter as compiled from multiple sources. The specific heat capacity of grey matter was taken to be $C = 3696$ J/kg/$^\circ$C, and the density of grey matter was assumed to be $\rho = 1045$ kg/m$^3$. The change in temperature was then estimated as $\Delta T = E/\rho C = 0.21^\circ$C. In arriving at this value, we have assumed that all of the absorbed light energy is eventually converted to heat.

**MRI and fMRI.** Imaging was performed with a Siemens Magnetom Skyra 3 Tesla scanner. All subjects wore protective eye goggles in addition to the laser headgear during scanning. A 16-channel transmit/receive head coil was used for data acquisition. Structural images were acquired with a T1-weighted MPRAGE sequence (FOV 230 mm, in plane resolution 256 x 256, 224 slices with a thickness of 0.9 mm, TI = 1000 ms). Functional BOLD scans were acquired with a multi-echo EPI sequence (FOV 228 mm, in plane resolution 90-by-90, 60 slices with a thickness of 2.5 mm, TR=2800 ms, Flip Angle = 82 degrees). The three echo times were 12.8 ms, 34.3 ms, and 55.6 ms, which allowed for the characterization of the T2$^*$ decay of the BOLD signal [49]. The duration of the BOLD scans was 30 minutes (645 volumes). Subjects were instructed to rest but stay awake and to not think about anything in particular.

**Interpolating light absorption onto human head.** In order to estimate the amount of light absorbed by the brain during tPBM, we interpolated the result from the simulation of light propagation (see *Simulating light propagation*) from the native simulation grid (two-dimensional radius $r$ and depth $z$, see Figure 1) onto the three-dimensional anatomy of each participant's head. This procedure was not aimed at circumventing the planar geometry of the simulation, but rather to allow for reasonable estimates of absorption in the brain, as well as the amount of light required to modulate BOLD. To that end, we manually extracted the coordinates of four points for each subject: the upper-right-front corner of the laser headgear, the upper-left-front corner, the upper-right-back corner, and the lower-right-front corner. Collectively, these points allowed for the computation of the position and orientation of the laser aperture. For each voxel in the MRI, we then computed its coordinates in a new two-dimensional space (radius and depth; note the cylindrical symmetry of the light absorption) referenced to the site of light incidence. The absorption at a given voxel was computed as the absorption at the simulation grid point with minimum Euclidean distance to the re-referenced voxel coordinate (nearest-neighbor interpolation). The same procedure was followed for the standard ("Colin 27") head [28], where we averaged the position and orientation of the laser aperture across subjects to define the site of light incidence on the standard head.

**fMRI Preprocessing.** Preprocessing of BOLD data was performed with the AfNI software package (Version 17.3.03) [15], scripted in the Matlab programming language (Mathworks, Natick, MA). The scripts are available at jd-lab.org/resources/laser.

The anatomical image was first skull-stripped using the *3dSkullStrip* function, whose output was then used to create a brain mask via the *3dAutomask* function. The anatomical image and brain mask were then registered to the Talairach atlas using the function *@auto_tlrc*.

To remove large transient spikes from the functional data, we applied the function *3dDespike* to the BOLD series of every voxel and echo. The operations of slice-time

correction, motion-correction, and alignment with the Talairach-registered anatomical MRI were then performed via the function *align_epi_anat.py*. Specifically, motion correction was performed by aligning each volume of the BOLD series to a reference volume (i.e., frame 5) using a 6-parameter rigid-body transformation. Registration of the functional images with the anatomical image was performed by a 12-parameter affine transformation maximizing the Local Pearson Correlation cost function.

A second stage of motion correction was then performed by regressing out the time series of the 6 alignment parameters computed in the first motion correction step (3 translation + 3 rotation), as well as its temporal derivatives. This involved projecting the multivariate BOLD onto the null space of the 12-dimensional time series. To further denoise the BOLD, we also regressed out the first 3 principal components of the white matter BOLD, a customary step based on the premise that the white matter represents a "nuisance" signal [11]. The BOLD was then low-pass filtered at 0.1 Hz, a conventional frequency cutoff for BOLD analysis [11]. The time series of each voxel and echo was z-scored. To adjust for small across-subject differences in the volume number corresponding to tPBM onset, we temporally aligned (via a circular shift) each subject's multivariate BOLD series so that the onset occurred at frame 215 (exactly 10 minutes).

We performed an additional spatial alignment step to each subject's BOLD data to enforce consistency in the region of the brain receiving tPBM. From the coordinates of each subject's headgear (see *Interpolating light absorption onto human head*), we computed the region-of-support of the interpolated absorption pattern (taken here as the spatial extent containing 99% of the total absorption). We then computed the centroid of this region and circularly shifted each subject's BOLD by the difference between their centroid and the mean centroid across subjects. Note that this step slightly moved each subject's anatomy out of the Talairach space, so that the effect of the tPBM could be coherently averaged across subjects.

After the temporal and spatial alignment, we computed the group average of the preprocessed BOLD. The motivation for performing an across-subject average (as opposed to conducting the whole-brain analysis at the level of each individual and then employing a second-level group analysis, as is common in conventional general linear model analyses) was to allow for the resolving of tPBM effects in our effectively single-trial data. In conventional event-related fMRI studies, one is afforded multiple repetitions of an experimental stimulus. Here, however, we were limited to a single application of the tPBM intervention, resulting in a low signal-to-noise ratio (SNR) in the individual BOLD traces. Averaging across subjects afforded us a SNR increase of $\sqrt{N} = \sqrt{20}$. Finally, the group average BOLD was smoothed to a FWHM of 8 mm using the AfNI function *3dBlurInMask*, yielding the final data that was analyzed for effects of tPBM. In order to obtain variability estimates for the analyzed group-averaged BOLD, we employed bootstrapping (sampling with replacement) along the $N = 20$ subject dimension. 100 bootstrap replicates of the group-averaged BOLD were generated such that standard deviations of the various BOLD statistics (signal intensity, AR spectra, and percent signal change) could be estimated.

**Chow Test for detecting an effect on BOLD.** To test for an effect of the tPBM on BOLD, we performed the Chow test, which detects the presence of a structural break in a time series [13]. The test is based on comparing the linear regression coefficients of two segments of a time series, thus providing a general test of significant differences (as opposed to simply testing whether one time series is higher or lower than another). To detect acute effects, we tested for significant differences between the pre-tPBM and peri-tPBM periods. To test for effects outlasting the stimulation, we tested for differences between the pre-tPBM and post-tPBM periods. For each period, we fit an autoregressive

(AR) model of the form: 457

$$y_v(t) = \sum_{k=1}^{p} a_{vk} y_v(t-k) + e_v(t), \tag{1}$$

where $y_v(t)$ is the BOLD signal of voxel $v$ at TR $t$, $a_{vk}$ is the autoregressive coefficient 458
of voxel $v$ at lag $k$, and $e_v(t)$ is a zero-mean additive white Gaussian error term. The 459
AR framework models each BOLD sample as a linear combination of the past $p$ samples 460
and a white noise error term. The rationale behind employing this model for BOLD is 461
that hemodynamics change slowly and are thus temporally redundant, yielding strong 462
autocorrelations in the signal. In other words, any part of the signal that is not predictable 463
from past values is likely noise. The signal captured by the AR model is precisely the 464
predictable signal. Separate tests were conducted at each BOLD echo, and all tests were 465
implemented using the Matlab function *chowtest*. 466

**Optimization of the AR model order.** In order to select the AR model order 467
employed in the Chow tests, we performed an optimization routine that spanned all 468
possible model orders from $p = 1$ to $p = 10$. For every voxel in the brain, we fit an 469
AR model of each order to the voxel's time series (all time series were normalized by 470
dividing the signal by its sum of squares). At each voxel and order, we employed a 5-fold 471
cross-validation procedure where 80% of the data was used to learn the AR coefficients, 472
while the remaining 20% was employed to measure the resulting residual signal (each 473
fold spanned a contiguous time segment). We conducted this procedure on the class of 474
models described in Eq. (1), and also those including a constant term: 475

$$y_v(t) = c + \sum_{k=1}^{P} a_{vk} y_v(t-k) + e_v(t), \tag{2}$$

where $c$ was also fit by the procedure. At each model order, the power of the residual 476
signal was averaged over all voxels, folds, and echos. We found slightly lower errors 477
with models that did not include the constant, and thus proceeded with only those 478
models. The selected model was chosen by identifying the knee point of the curve of 479
mean residual versus model order, which occurred at $p = 4$ (Fig S1), matching the value 480
found by [27]. While slightly lower errors were found at higher orders (5 to 7), this 481
selection represented a more parsimonious model that was less likely to produce spurious 482
detection, which is expected to increase with the number of AR coefficients. 483

**Whole-Brain Analysis.** Chow tests were conducted independently at each voxel. To 484
correct for multiple comparisons, we controlled for the False Discovery Rate (FDR) at a 485
level of $\alpha = 0.05$ ($N = 86,851$ comparisons, one for each voxel in the standard brain). 486
Significant voxels that survived FDR correction were then pruned to retain only those 487
belonging to a cluster of at least 40 voxels (625 mm$^3$), where a cluster was defined as a 488
set of voxels such that each voxel in the cluster was less than 2.5 mm (center-to-center 489
distance) to at least one other voxel in the cluster. 490

**Computation of AR spectrum.** To gain insight into the nature of the tPBM effect 491
on the BOLD signal (increase versus decrease, low- versus high-frequency), we computed 492
the spectra of the BOLD captured by the AR models employed in the Chow tests. For 493
each of the three time segments (pre-, peri-, and post-tPBM), we computed the AR 494
spectra according to: 495

$$A_v(l) = \frac{1}{1 - \sum_{k=1}^{N} a_{vk} e^{-j2\pi lk/N}}, \tag{3}$$

where $A_v(l)$ is the spectral coefficient at frequency $2\pi l/N$, $a_{vk}$ is the fitted AR coefficient of lag $k$ and voxel $v$ (see Eq. 1), and $N = 32$ is the length of the Fast Fourier Transform. Note that by construction, $a_{v0} = 1$ [9]. The signal recovered by the AR model may be viewed as the output of a linear filter whose frequency response is given by $A_v(l)$ to a white noise input. We thus compared the magnitudes of $A_v(l)$ between the three temporal segments of the experiment.

**Analysis of BOLD effect size versus echo time**  To test whether the effect of tPBM on BOLD exhibited a linear dependence on echo time, we considered voxels exhibiting a significant acute effect at any of the 3 echos. There were $N = 258$ such voxels. For each of these, we computed the percent signal change (frequency-weighted average of the AR spectral magnitude), then computed the average percent signal change across voxels, and finally regressed the result onto echo time using ordinary least squares. To test for a significant linear dependence of percent signal change on echo time, we compared two linear regression models. The "full" model was specified by:

$$\mathrm{PSC}(t) = bt + b_o \qquad (4)$$

where $\mathrm{PSC}(t)$ is the percent signal change at echo time $t$, $b$ is the slope and $b_o$ the y-intercept. The residual error of the full model was contrasted to that given by the following "reduced" model:

$$F(t) = b_o, \qquad (5)$$

where a general linear F-test was conducted to evaluate whether the full model significantly reduces the residual over the reduced model.

**Logistic regression analysis.**  To obtain estimates of the amount of light that is required to modulate the BOLD signal, we conducted a classification analysis aimed at predicting whether a given brain region exhibited a significant modulation during tPBM. For this analysis, we resampled the pattern of significant voxels (i.e., results of the Chow tests) onto the anatomical space of the standard head [28] where the absorption was defined. Voxels were then split into two classes: those exhibiting a significant effect (after FDR correction and clustering), and those that did not. Voxels outside of the brain and those having zero absorption (i.e., locations very far from the site of stimulation) were excluded from the analysis. For the analysis of echo 3, we also excluded voxels in the significant clusters residing in the paracentral lobule and cerebellum which were presumed to be related to movement (see Table 1). This led to the following number of voxels in each echo: 3555 significant and 212384 not-significant (Echo 1), 2433 significant and 213506 not-significant (Echo 2), 890 significant and 215049 not-significant (Echo 3). Due to the large imbalance in the sizes of the two classes, we employed a common technique in class-imbalanced learning problems, namely repeating the infrequent examples (i.e., significant voxels) such that the number of examples in each class was equal [38]. We then fit a simple classifier of the form:

$$p(\text{significant}) = \frac{1}{1 + e^{-(\beta a + \beta_o)}}, \qquad (6)$$

where $a$ is the absorption, $\beta$ is the linear term multiplying the absorption, and $\beta_o$ is the threshold which represents the optimal decision boundary between predictions of significant and non-significant voxels. At each echo, learning of the model parameters $\beta$ and $\beta_o$ was performed by the Matlab function *mnrfit* [40]. From the logistic regression model, we estimated the absorption required to achieve a BOLD effect with probabilities of 0.5 and 0.95 by setting $p(\text{significant})$ to the desired probability and then solving for $a$ in Eq. (6).

**Simulation of BOLD signal changes.**                                                   539

In order to demonstrate the combined effects of increased CBF and OEF, we conducted   540
a simple simulation of the BOLD signal:                                               541

$$S(t) = S_o(t)e^{-t/T_2^*}. \tag{7}$$

Baseline values were selected as $S_o = 1$ and $T_2^* = 0.035$. We simulated a 40% increase in   542
$S_o$, a 10% decrease in T2$^*$, as well as their combined effect.                     543

# References

1. Tissue properties. https://itis.swiss/virtual-population/tissue-properties/database/heat-capacity/. Accessed: 2018-10-15.

2. Tissue properties. https://itis.swiss/virtual-population/tissue-properties/database/density/. Accessed: 2018-10-15.

3. A. Ascenzi and C. Fabry. Technique for dissection and measurement of refractive index of osteones. *J Biophys Biochem Cytol*, 6(1):139–142, Aug 1959. 13673068[pmid].

4. D. Attwell and S. B. Laughlin. An energy budget for signaling in the grey matter of the brain. *Journal of Cerebral Blood Flow & Metabolism*, 21(10):1133–1145, 2001.

5. D. Barrett and F. Gonzalez-Lima. Transcranial infrared laser stimulation produces beneficial cognitive and emotional effects in humans. *Neuroscience*, 230:13–23, 2013.

6. L. R. Baxter, J. M. Schwartz, M. E. Phelps, J. C. Mazziotta, B. H. Guze, C. E. Selin, R. H. Gerner, and R. M. Sumida. Reduction of prefrontal cortex glucose metabolism common to three types of depression. *Archives of general psychiatry*, 46(3):243–250, 1989.

7. N. J. Blanco, W. T. Maddox, and F. Gonzalez-Lima. Improving executive function using transcranial infrared laser stimulation. *Journal of neuropsychology*, 11(1):14–25, 2017.

8. N. J. Blanco, C. L. Saucedo, and F. Gonzalez-Lima. Transcranial infrared laser stimulation improves rule-based, but not information-integration, category learning in humans. *Neurobiology of learning and memory*, 139:69–75, 2017.

9. G. E. Box, G. M. Jenkins, G. C. Reinsel, and G. M. Ljung. *Time series analysis: forecasting and control*. John Wiley & Sons, 2015.

10. R. B. Buxton. The physics of functional magnetic resonance imaging (fmri). *Reports on Progress in Physics*, 76(9):096601, 2013.

11. C. Caballero-Gaudes and R. C. Reynolds. Methods for cleaning the bold fmri signal. *Neuroimage*, 154:128–149, 2017.

12. P. Cassano, S. R. Petrie, M. R. Hamblin, T. A. Henderson, and D. V. Iosifescu. Review of transcranial photobiomodulation for major depressive disorder: targeting brain metabolism, inflammation, oxidative stress, and neurogenesis. *Neurophotonics*, 3(3):031404, 2016.

13. G. C. Chow. Tests of equality between sets of coefficients in two linear regressions. *Econometrica: Journal of the Econometric Society*, pages 591–605, 1960.

14. H. Chung, T. Dai, S. K. Sharma, Y.-Y. Huang, J. D. Carroll, and M. R. Hamblin. The nuts and bolts of low-level laser (light) therapy. *Annals of biomedical engineering*, 40(2):516–533, 2012.

15. R. W. Cox. Afni: software for analysis and visualization of functional magnetic resonance neuroimages. *Computers and Biomedical research*, 29(3):162–173, 1996.

16. J. C. de la Torre. Is alzheimer's disease a neurodegenerative or a vascular disorder? data, dogma, and dialectics. *The Lancet Neurology*, 3(3):184–190, 2004.

17. L. De Taboada, J. Yu, S. El-Amouri, S. Gattoni-Celli, S. Richieri, T. McCarthy, J. Streeter, and M. S. Kindy. Transcranial laser therapy attenuates amyloid-$\beta$ peptide neuropathology in amyloid-$\beta$ protein precursor transgenic mice. *Journal of Alzheimer's disease*, 23(3):521–535, 2011.

18. H. Ding, J. Q. Lu, W. A. Wooden, P. J. Kragel, and X.-H. Hu. Refractive indices of human skin tissues at eight wavelengths and estimated dispersion relations between 300 and 1600 nm. *Physics in medicine and biology*, 51(6):1479, 2006.

19. D. Farfara, H. Tuby, D. Trudler, E. Doron-Mandel, L. Maltz, R. J. Vassar, D. Frenkel, and U. Oron. Low-level laser therapy ameliorates disease progression in a mouse model of alzheimer's disease. *Journal of Molecular Neuroscience*, 55(2):430–436, 2015.

20. M. Firbank, M. Hiraoka, M. Essenpreis, and D. Delpy. Measurement of the optical properties of the skull in the wavelength range 650-950 nm. *Physics in medicine and biology*, 38(4):503, 1993.

21. J. Frahm, K.-D. Merboldt, W. Hänicke, A. Kleinschmidt, and H. Boecker. Brain or vein? oxygenation or flow? on signal physiology in functional mri of human brain activation. *NMR in Biomedicine*, 7(1-2):45–53, 1994.

22. V. C. Hachinski, L. D. Iliff, E. Zilhka, G. H. Du Boulay, V. L. McAllister, J. Marshall, R. W. R. Russell, and L. Symon. Cerebral blood flow in dementia. *Archives of neurology*, 32(9):632–637, 1975.

23. F. B. Haeussinger, S. Heinzel, T. Hahn, M. Schecklmann, A.-C. Ehlis, and A. J. Fallgatter. Simulation of near-infrared light absorption considering individual head and prefrontal cortex anatomy: implications for optical neuroimaging. *PloS one*, 6(10):e26377, 2011.

24. M. R. Hamblin. Shining light on the head: photobiomodulation for brain disorders. *BBA clinical*, 6:113–124, 2016.

25. M. R. Hamblin. Mechanisms and applications of the anti-inflammatory effects of photobiomodulation. *AIMS Biophys*, 4(3):337–361, 2017.

26. M. R. Hamblin and T. N. Demidova. Mechanisms of low level light therapy. In *Mechanisms for low-light therapy*, volume 6140, page 614001. International Society for Optics and Photonics, 2006.

27. L. Harrison, W. D. Penny, and K. Friston. Multivariate autoregressive modeling of fmri time series. *Neuroimage*, 19(4):1477–1491, 2003.

28. C. J. Holmes, R. Hoge, L. Collins, R. Woods, A. W. Toga, and A. C. Evans. Enhancement of mr images using registration for signal averaging. *Journal of computer assisted tomography*, 22(2):324–333, 1998.

29. Y.-Y. Huang, A. C.-H. Chen, J. D. Carroll, and M. R. Hamblin. Biphasic dose response in low level light therapy. *Dose Response*, 7(4):358–383, Sep 2009.

30. J. Hwang, D. M. Castelli, and F. Gonzalez-Lima. Cognitive enhancement by transcranial laser stimulation and acute aerobic exercise. *Lasers in medical science*, 31(6):1151–1160, 2016.

31. S. L. Jacques. Optical properties of biological tissues: a review. *Physics in Medicine and Biology*, 58(11):R37, 2013.

32. H. Jasper. Report of the committee on methods of clinical examination in electroencephalography. *Electroencephalogr Clin Neurophysiol*, 10:370–375, 1958.

33. T. Karu. Mechanisms of low-power laser light action on cellular level. In *Proc SPIE*, volume 4159, pages 1–17, 2000.

34. P. Kundu, S. J. Inati, J. W. Evans, W.-M. Luh, and P. A. Bandettini. Differentiating bold and non-bold signals in fmri time series using multi-echo epi. *Neuroimage*, 60(3):1759–1770, 2012.

35. V. Lebon, P. G. Carlier, C. Brillault-Salvat, and A. Leroy-Willig. Simultaneous measurement of perfusion and oxygenation changes using a multiple gradient-echo sequence: application to human muscle study. *Magnetic resonance imaging*, 16(7):721–729, 1998.

36. P. Limousin, P. Krack, P. Pollak, A. Benazzouz, C. Ardouin, D. Hoffmann, and A.-L. Benabid. Electrical stimulation of the subthalamic nucleus in advanced parkinson's disease. *New England Journal of Medicine*, 339(16):1105–1111, 1998.

37. Y. Lu, R. Wang, Y. Dong, D. Tucker, N. Zhao, M. E. Ahmed, L. Zhu, T. C.-Y. Liu, R. M. Cohen, and Q. Zhang. Low-level laser therapy for beta amyloid toxicity in rat hippocampus. *Neurobiology of aging*, 49:165–182, 2017.

38. M. A. Maloof. Learning when data sets are imbalanced and when costs are unequal and unknown. In *ICML-2003 workshop on learning from imbalanced data sets II*, volume 2, pages 2–1, 2003.

39. G. Marchal, P. Rioux, M.-C. Petit-Taboué, G. Sette, J.-M. Travère, C. Le Poec, P. Courtheoux, J.-M. Derlon, and J.-C. Baron. Regional cerebral oxygen consumption, blood flow, and blood volume in healthy human aging. *Archives of neurology*, 49(10):1013–1020, 1992.

40. P. McCullagh and J. A. Nelder. *Generalized linear models*, volume 37. CRC press, 1989.

41. E. Mester, B. Szende, J. Tota, et al. Effect of laser on hair growth of mice. *Kiserl Orvostud*, 19:628–631, 1967.

42. N. Mochizuki-Oda, Y. Kataoka, Y. Cui, H. Yamada, M. Heya, and K. Awazu. Effects of near-infra-red laser irradiation on adenosine triphosphate and adenosine diphosphate contents of rat brain tissue. *Neuroscience letters*, 323(3):207–210, 2002.

43. M. S. Moreira, I. T. Velasco, L. S. Ferreira, S. K. K. Ariga, D. F. Barbeiro, D. T. Meneguzzo, F. Abatepaulo, and M. M. Marques. Effect of phototherapy with low intensity laser on local and systemic immunomodulation following focal brain damage in rat. *Journal of Photochemistry and Photobiology B: Biology*, 97(3):145–151, 2009.

44. P. I. Moreira, C. Carvalho, X. Zhu, M. A. Smith, and G. Perry. Mitochondrial dysfunction is a trigger of alzheimer's disease pathophysiology. *Biochimica et Biophysica Acta (BBA)-Molecular Basis of Disease*, 1802(1):2–10, 2010.

45. S. Ogawa, T.-M. Lee, A. R. Kay, and D. W. Tank. Brain magnetic resonance imaging with contrast dependent on blood oxygenation. *Proceedings of the National Academy of Sciences*, 87(24):9868–9872, 1990.

46. E. Okada and D. T. Delpy. Near-infrared light propagation in an adult head model. ii. effect of superficial tissue thickness on the sensitivity of the near-infrared spectroscopy signal. *Applied optics*, 42(16):2915–2921, 2003.

47. A. Pascual-Leone, B. Rubio, F. Pallardó, and M. D. Catalá. Rapid-rate transcranial magnetic stimulation of left dorsolateral prefrontal cortex in drug-resistant depression. *The Lancet*, 348(9022):233–237, 1996.

48. A. Pitzschke, B. Lovisa, O. Seydoux, M. Zellweger, M. Pfleiderer, Y. Tardy, and G. Wagnières. Red and nir light dosimetry in the human deep brain. *Physics in Medicine & Biology*, 60(7):2921, 2015.

49. S. Posse, S. Wiese, D. Gembris, K. Mathiak, C. Kessler, M.-L. Grosse-Ruyken, B. Elghahwagi, T. Richards, S. R. Dager, and V. G. Kiselev. Enhancement of bold-contrast sensitivity by single-shot multi-echo functional mr imaging. *Magnetic resonance in medicine*, 42(1):87–97, 1999.

50. S. Prahl. *Light transport in tissue*. PhD thesis, University of Texas, Austin, Texas, 1988.

51. R. J. Racine. Modification of seizure activity by electrical stimulation: Ii. motor seizure. *Electroencephalography and clinical neurophysiology*, 32(3):281–294, 1972.

52. R. L. Rungta, B.-F. Osmanski, D. Boido, M. Tanter, and S. Charpak. Light controls cerebral blood flow in naive animals. *Nature communications*, 8:14191, 2017.

53. F. Salehpour, N. Ahmadian, S. H. Rasta, M. Farhoudi, P. Karimi, and S. Sadigh-Eteghad. Transcranial low-level laser therapy improves brain mitochondrial function and cognitive impairment in d-galactose–induced aging mice. *Neurobiology of aging*, 58:140–150, 2017.

54. F. Salehpour, F. Farajdokht, M. Erfani, S. Sadigh-Eteghad, S. S. Shotorbani, M. R. Hamblin, P. Karimi, S. H. Rasta, and J. Mahmoudi. Transcranial near-infrared photobiomodulation attenuates memory impairment and hippocampal oxidative stress in sleep-deprived mice. *Brain research*, 1682:36–43, 2018.

55. J. L. Sandell and T. C. Zhu. A review of in-vivo optical properties of human tissues and its impact on pdt. *J Biophotonics*, 4(11-12):773–787, Nov 2011. 22167862[pmid].

56. F. E. W. Schmidt. Development of a time-resolved optical tomography system for neonatal brain imaging. *Medical Physics*, 27(6):1343–1343.

57. M. G. Shapiro, K. Homma, S. Villarreal, C.-P. Richter, and F. Bezanilla. Infrared light excites cells by changing their electrical capacitance. *Nature communications*, 3:736, 2012.

58. C. E. Tedford, S. DeLapp, S. Jacques, and J. Anders. Quantitative analysis of transcranial and intraparenchymal light penetration in human cadaver brain tissue. *Lasers in surgery and medicine*, 47(4):312–322, 2015.

59. F. Tian, S. N. Hase, F. Gonzalez-Lima, and H. Liu. Transcranial laser stimulation improves human cerebral oxygenation. *Lasers in surgery and medicine*, 48(4):343–349, 2016.

60. Y. Uozumi, H. Nawashiro, S. Sato, S. Kawauchi, K. Shima, and M. Kikuchi. Targeted increase in cerebral blood flow by transcranial near-infrared laser irradiation. *Lasers in surgery and medicine*, 42(6):566–576, 2010.

61. L. Wang, S. L. Jacques, and L. Zheng. Mcml—monte carlo modeling of light transport in multi-layered tissues. *Computer methods and programs in biomedicine*, 47(2):131–146, 1995.

62. M. T. Wong-Riley, H. L. Liang, J. T. Eells, B. Chance, M. M. Henry, E. Buchmann, M. Kane, and H. T. Whelan. Photobiomodulation directly benefits primary neurons functionally inactivated by toxins role of cytochrome c oxidase. *Journal of Biological Chemistry*, 280(6):4761–4771, 2005.

63. D. A. Yablonskiy, J. J. Ackerman, and M. E. Raichle. Coupling between changes in human brain temperature and oxidative metabolism during prolonged visual stimulation. *Proceedings of the National Academy of Sciences*, 97(13):7603–7608, 2000.

64. T. Yamaguchi, I. Kanno, K. Uemura, F. Shishido, A. Inugami, T. Ogawa, M. Murakami, and K. Suzuki. Reduction in regional cerebral metabolic rate of oxygen during human aging. *Stroke*, 17(6):1220–1228, 1986.

65. Z. Yu, Z. Li, N. Liu, Y. Jizhang, T. J. McCarthy, C. E. Tedford, E. H. Lo, and X. Wang. Near infrared radiation protects against oxygen-glucose deprivation-induced neurotoxicity by down-regulating neuronal nitric oxide synthase (nnos) activity in vitro. *Metabolic brain disease*, 30(3):829–837, 2015.

66. Q. Zhang, C. Zhou, M. R. Hamblin, and M. X. Wu. Low-level laser therapy effectively prevents secondary brain injury induced by immediate early responsive gene x-1 deficiency. *Journal of Cerebral Blood Flow & Metabolism*, 34(8):1391–1401, 2014.

| Layer | Refractive Index | Absorption Coefficient ($\mu_a$) | Scattering Coefficient ($\mu_s$) | Anisotropy Factor ($g$) | Thickness (cm) |
|---|---|---|---|---|---|
| Scalp | 1.41 [18] | 0.2 [55] | 31.25 [55] | 0.52 [50] | 0.6 [46] |
| Skull | 1.56 [3] | 0.07 [55] | 130 [55] | 0.9 [20] | 0.65 [46] |
| CSF | 1.33 [31] | 0.02 [46] | 0.1 [46] | 0.9 [56] | 0.2 [46] |
| Parenchyma | 1.4 [31] | 0.084 [55] | 90 [55] | 0.9 [31] | 8 [46] |

**Table S1.** Physical and optical properties of the four-layer head model employed in the simulation of light propagation. Values of $\mu_a$ and $\mu_s$ are given in units of cm$^{-1}$.
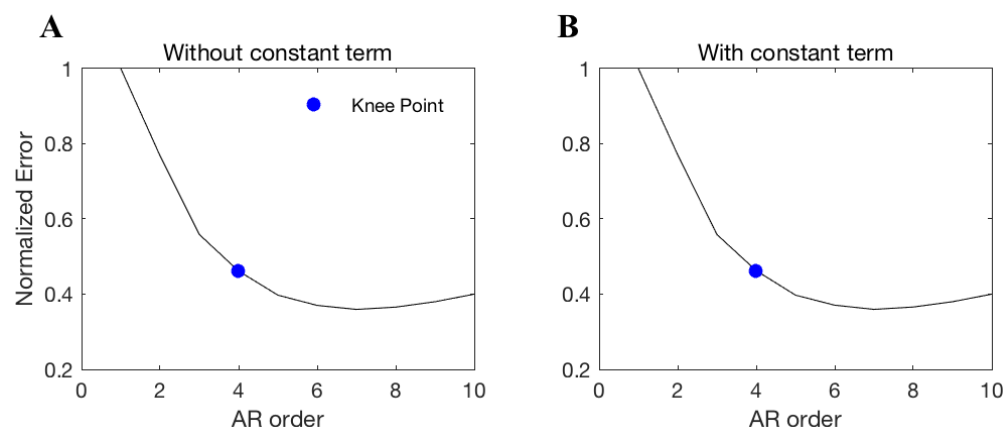
**Figure S1.** Optimization of the AR model order based on minimizing the residual. The BOLD series of every brain voxel was fit to AR models of varying order (1 to 10) using ordinary least squares. For each order, the power of the residual error signal was computed on unseen "test" data. (**A**) After averaging across voxels and normalizing, the error decreased rapidly at low orders and exhibited a knee point at $p = 4$, which was the model order employed in the rest of the study. (**B**) Same as (A) but now including a constant term in the AR model. The inclusion of the constant did not decrease error which was actually slightly increased. As a result, a constant term was not employed in the study.
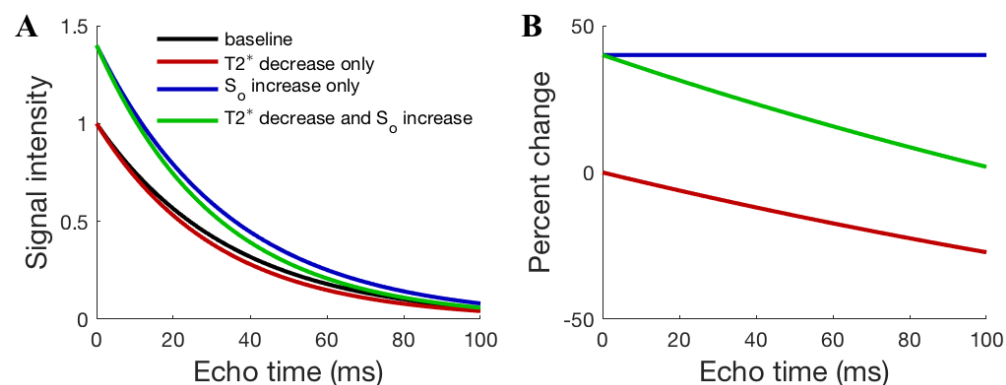


**Figure S2.** Observed BOLD modulation is consistent with a simultaneous decrease in $T_2^*$ and increase in initial signal intensity $S_o$. (**A**) Simulated Free Induction Decay (FID) signal $S(t) = S_o e^{-t/T_2^*}$ in the baseline state (black), showing a 10% decrease in $T_2^*$ (red), a 40 % increase in $S_o$ (blue), and both (green). (**B**) The percent signal change from the individual and combined modulations: a combined decrease in $T_2^*$ and increase in $S_o$ shows the pattern of signal change observed in the BOLD experiments.